Passage of millicharged particles in the electron beam-dump: Refining constraints from SLACmQ and estimating sensitivity of NA64*e*

Nataliya Arefyeva,[1,2] Sergei Gninenko,[2] Dmitry Gorbunov,[2,3] and Dmitry Kirpichnikov[2]
[1]*Physical Department, Lomonosov Moscow State University, Vorobiovy Gory, Moscow 119991, Russia*
[2]*Institute for Nuclear Research of the Russian Academy of Sciences, 117312 Moscow, Russia*
[3]*Moscow Institute of Physics and Technology, Institutsky lane 9, Dolgoprudny, Moscow region, 141700, Russia*

(Received 21 April 2022; accepted 3 August 2022; published 25 August 2022)

Millicharged particles (MCPs) arise in many well-motivated extensions of the Standard Model and are a popular subject for experimental searches. We investigate the attenuation of the MCP flux produced at accelerator experiments due to their interactions in the media and demonstrate that it can significantly affect the final sensitivity to the MCP parameter space, leaving its essential part still unexplored. Applying our analysis to the SLACmQ experiment [A. A. Prinz *et al.*, Phys. Rev. Lett. **81**, 1175 (1998)], we correct their published exclusion bounds; the obtained results are numerically in a good accordance with A. A. Prinz [Report No. SLAC-R-569]. We also show that this newly reopened area with the MCP masses in the range 10^{-4} eV–1 GeV and charges $\gtrsim 10^{-5}e$ can be effectively probed by the NA64*e* experiment at the CERN SPS. Light MCPs are mostly produced by a virtual photon in electron scattering off nuclei. The main source of heavy MCP is decays of vector mesons, produced by the electrons on nuclei.

DOI: 10.1103/PhysRevD.106.035029

I. INTRODUCTION

Millicharged particles (MCPs) are considered in connection with the electric charge quantization mechanism and new physics models with electric charge nonconservation [1]. Moreover, scenarios beyond the Standard Model (SM) of particle physics can naturally include particles, whose electric charge is a small fraction of the electron's charge, $Q_\chi = e\epsilon \ll e$. In particular, the millicharged particles can be considered as well-motivated dark-matter candidates [2–8]. Thus, experimental searches for such particles are of great interest [9].

The simplest way to introduce the MCPs in a model is to consider them as a low-energy limit of the theory, where a hidden (dark) photon, A'_μ, kinetically mixes with the visible SM photon A_μ [10]. As a result, e.g., a new fermion of the hidden sector χ, coupled to the hidden photon, can acquire a small electric charge $\sim e\epsilon$, and the model Lagrangian can be written as follows:

$$\mathcal{L} \supset i\bar{\chi}\gamma^\mu\partial_\mu\chi - m_\chi\bar{\chi}\chi + e\epsilon A_\mu\bar{\chi}\gamma^\mu\chi, \tag{1}$$

where m_χ is the Dirac mass of the hidden MCP.

The parameter space of the MCP on the (ϵ, m_χ) plane can be constrained from the searches at collider [11–19] and fixed-target [20–28] experiments, with optical sensors [29–31] and searches with a superconducting radio frequency cavity [32], from analysis of cosmological and astrophysical observations [33–45], and by using results of cosmic-ray detectors [46–48] and nuclear reactor experiments [49–51], etc.

In accelerator experiments, the MCPs can be produced at intense proton fixed-target facilities in decays of mesons,

$$\pi^0, \eta, \eta' \to \gamma\chi\bar{\chi}, \qquad \rho, \omega, \phi, J/\psi \to \chi\bar{\chi}, \tag{2}$$

from hadronic showers initiated by high-energy protons in a dump. A thick shield between the production and detection points of the MCP absorbs all strongly and electromagnetically interacting secondary particles, while the MCP may pass through the shield and can be detected in a far detector via their scattering off electrons, $\chi e^- \to \chi e^-$. In this case, the observation of MCP is based on a search for an excess of low-energy recoil electrons in the detector. The number of signal events N_χ in such type of experiments, scales as $N_\chi \propto \epsilon^4$ for a single MCP hit in the detector, and as $N_\chi \propto \epsilon^6$ for the double-hit MCP signature [23]. Consequently, a large number of protons on target (POT) is required to probe small values of ϵ. For example, for, say, $\epsilon \lesssim 10^{-3}$ and MCP masses $m_\chi \gtrsim 100$ MeV, one needs $\sim\mathcal{O}(10^{20})$–$\mathcal{O}(10^{22})$ POT.

A more powerful and effective approach of probing MCP can be based on their production in high-energy electrons scattering off heavy nuclei, the process exploited by the NA64*e* experiment in the north area of the CERN SPS. The NA64*e* facility has been originally designed for searching for light dark matter (LDM) production in invisible decays of a dark photon (A') mediator in the reaction chain, $e^-N \to e^-NA'$; $A' \to \text{LDM}$ [52]. That approach can be also adopted for searching for MCP in missing energy events due to the MCP production in the reaction $eN \to e^-N\gamma^* \to e^-N\chi\bar{\chi}$ accompanied by missing energy carried away by the MCP pair. The expected number of signal events in this case is proportional to $N_\chi \propto \epsilon^2$. Therefore, a much lower number of electrons on target (EOT), $n_{\text{EOT}} \simeq \mathcal{O}(10^{12})$–$\mathcal{O}(10^{13})$ is required to test the same region at small values $\epsilon \lesssim 10^{-3}$ [52] as compared to the required number of POT.

Another point, discussed in this work, is related to the attenuation of a charged particle flux while propagating in the matter. Both the energy losses and multiple scattering of charged particles strongly depend on the their charge-to-mass ratio, as we well know from the comparison of the electron and muon propagation in media. Therefore, for the relatively light MCP in the mass range, $m_\chi \lesssim 10$ MeV, and a small charge $\epsilon \lesssim 10^{-5}$–$10^{-1}$, the search sensitivity of beam-dump experiments, such, e.g., as SLACmQ [53], might be constrained by a significant attenuation of the MCP flux at the detector location.

Investigating SLACmQ in this paper, we rely on the MCP yield provided by Ref. [54] for SLAC. In particular, in our analysis, we adopt the exclusion limits associated with MCP that would reach the SLAC detector without energy loss [54]. The adopted exclusion limit corresponds to the SLAC lower edge curve of Fig. 5.17 from Ref. [54]. By using both the numerical MCP spectra and former SLAC limit, we recalculated numerically the part of the MCP bounds from the SLACmQ beam-dump experiment taking into account the MCP flux attenuation due to (i) MCP energy loss in the reactions of $\chi e^- \to \chi e^-$ scattering, pair production, $\chi N \to \chi N e^+ e^-$, bremsstrahlung, $\chi N \to \chi N \gamma$ (ii) timing acceptance, and (iii) decreasing of the MCP deflection acceptance due to the MCP multiple scattering in the dump.

We show that indeed, altogether these processes may prevent the MCP from reaching the SLAC mQ detector and giving the signal. We find that our revised results on SLAC MCP sensitivity following from the processes (i)–(iii) are in a fairly good agreement with previous study [54], which corresponds to the upper edge curve of Fig. 5.17 from Ref. [54].

We implement the developed ideas of MCP stopping power calculation for the estimate of the expected reach of the NA64*e* in the region of model parameter space, $m_\chi \lesssim$ 100 MeV and $\epsilon \lesssim 10^{-5}$–$10^{-1}$. We also calculate and find it promising the expected sensitivity of NA64*e* to MCP, produced in bremsstrahlung-like events, $eN \to eN\gamma^*(\to\chi\bar{\chi})$ and to MCP, emerged in invisible decays of short-lived vector mesons $V = \{\rho, \omega, \phi, J/\psi\}$, produced in the reaction of photo-production inside the dump, $\gamma^*N \to NV(\to\chi\bar{\chi})$ for $m_\chi \gtrsim 10$ MeV and $10^{-3} \lesssim \epsilon \lesssim 10^{-2}$.

The paper is structured as follows. Section II describes various effects associated with MCP passage through matter, namely: the dominant MCP energy losses in the matter (ionization and radiation losses via bremsstrahlung and e^+e^- pair production) and the deflection of MCP trajectory due to multiple scattering. In Sec. III, we implement the results of Sec. II to revise the analysis of the SLACmQ experiment [53] and correct their exclusion region in (m_χ, ϵ) parameter space. In Sec. IV, we calculate the exact tree-level cross section of the process $eN \to eN\gamma^*(\to\chi\bar{\chi})$ to estimate the yield of the MCP in the NA64*e* missing energy signature. In Sec. V, we estimate the NA64*e* prospects in probing MCP models for the relatively wide mass range 10^{-4} eV $\lesssim m_\chi \lesssim 1$ GeV. In Sec. VI, we estimate the expected reach of the NA64*e* to examine MCPs from invisible decay of vector mesons. We conclude in Sec. VII. Two appendixes contain some formulas used in the numerical calculations.

II. MCP INTERACTIONS IN MATTER

High energy particles can produce sufficiently light MCPs by scattering off the target. In turn, the MCP collides with electrons and nuclei of the dump material resulting in energy losses and multiple scattering, and thus, deviation from its original direction, when passing through matter. In this section, we consider three processes of MCP energy loses: ionization, radiation, and pair production, some of which are illustrated in Fig. 1. In the end of section, we estimate a typical angle of MCP deviation from the original direction due to the multiple scattering.

A. Ionization losses

Ionization energy losses are associated with the MCP collision with an atom, which initiates the atom excitation and knocking out the electron; see Fig. 1(a1). To quantify the ionization losses effect for MCP, we adopt the Bethe-Bloch formula as [55]

$$\left(-\frac{dE_\chi}{dx}\right)_{\text{ion}} = \frac{4\pi Z\epsilon^2 r_e^2 m_e}{\beta_\chi^2}\frac{N_A\rho}{M_A} \times \left(\frac{1}{2}\ln\frac{2m_e\beta_\chi^2\gamma_\chi^2 T_{\max}}{I^2} - \beta_\chi^2 - \frac{\delta(\beta_\chi\gamma_\chi)}{2}\right), \quad (3)$$

where x is the track length of MCP, β_χ is its velocity, and $\gamma_\chi = E_\chi/m_\chi$ is its Lorentz factor. The last term in (3) comes from the matter polarization, and at very high energies, $\gamma_\chi \gg 1$, it approaches $\delta(\beta_\chi\gamma_\chi) \approx 2\log(\omega_p\beta_\chi\gamma_\chi/I) - 1$. Then I stands for the ionization potential of the atom,

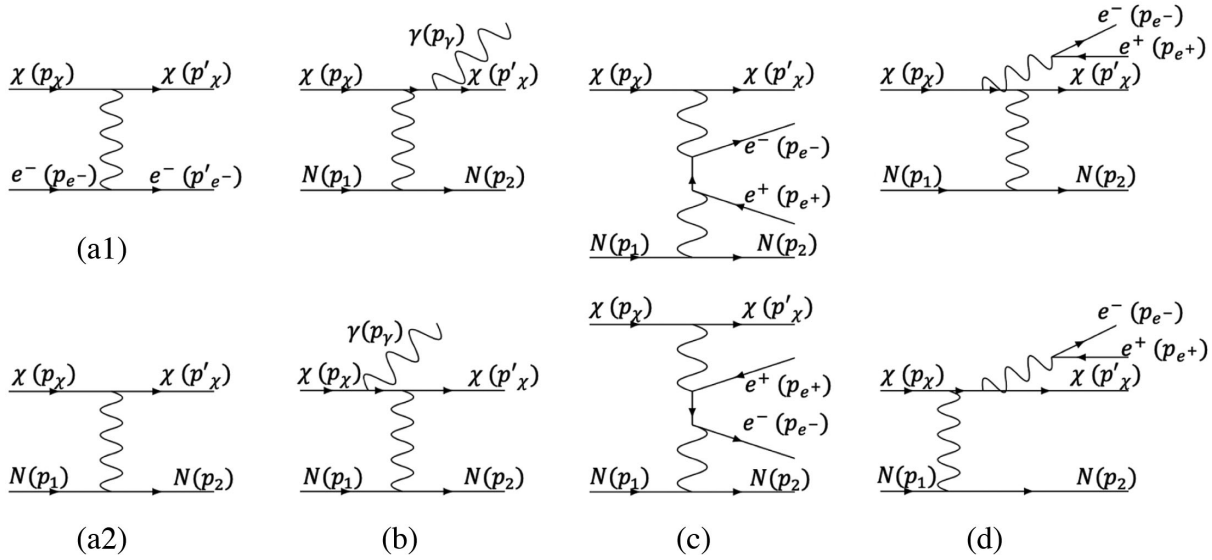

FIG. 1. Feynman diagrams for MCP energy loss in matter: (a) scattering off atomic nucleus and electrons, (b) bremsstrahlung, (c), (d) e^+e^- pair production.

$r_e = \alpha/m_e \simeq 2.8$ fm is the classical radius of the electron, $N_A = 6.02 \times 10^{23}$ mol^{-1} is the Avogadro's number, Z is the atomic number of target material, M_A is the atomic mass of the target material, and ρ is its density, the maximum energy transferred from MCP to an electron is given by

$$T_{\max} = \frac{2m_e\beta_\chi^2\gamma_\chi^2}{1 + 2\gamma_\chi m_e/m_\chi + m_e^2/m_\chi^2}. \tag{4}$$

We note that the MCP's ionization stopping power (3) scales as $\propto \epsilon^2$ and depends logarithmic on E_χ and m_χ in the ultrarelativistic regime $\beta_\chi \simeq 1$.

B. Radiation losses

The MCP slows down due to the scattering off nuclei in the material and the emission of photons as illustrated by the Feynman diagrams in Fig. 1(b). The radiation loss due to scattering off electrons is suppressed by the nuclear charge as $1/Z$, and we neglect it in our study.

The atomic electrons outside the nucleus screen the nucleus Coulomb field, so that its effective strength decreases and atomic electrons also serve as scattering targets. In our case of ultrarelativistic MCP, the screening can be considered as a complete one. The MCP energy losses for radiation per unit length are determined by

$$\left(-\frac{dE_\chi}{dx}\right)_{\text{brems}} = n\int_0^{E_\chi - m_\chi} dE_\gamma \frac{d\sigma_{\text{brems}}}{dE_\gamma} E_\gamma, \tag{5}$$

where $n = N_A\rho/M_A$ is the number density of atoms in the target, $d\sigma_{\text{brems}}/dE_\gamma$ is the differential bremsstrahlung cross section, and E_γ is the energy of the emitted photon. The bremsstrahlung spectrum in the case of complete screening is given by the formula [55],

$$\frac{d\sigma_{\text{brems}}}{dE_\gamma} \simeq \frac{1}{E_\gamma} 4\alpha Z^2 r_e^2 \epsilon^4 \left(\frac{m_e}{m_\chi}\right)^2 \left(\frac{4}{3} - \frac{4}{3}\frac{E_\gamma}{E_\chi} + \frac{E_\gamma^2}{E_\chi^2}\right) F_{\text{corr}}, \tag{6}$$

where F_{corr} is the factor that takes into account the Coulomb correction to the Born cross section and atomic screening effects [55]. We note that the stopping loss of the MCP due to the radiation scales as $\propto \epsilon^4 E_\chi/m_\chi^2$; therefore, the lighter MCPs lose their energy more rapidly.

C. Electron-positron pair production

MCP energy losses can be accounted by considering the process illustrated in Figs. 1(c) and 1(d). One observes, that for sufficiently small parameter ϵ, the amplitude of Fig. 1(d) is suppressed due to the additional factor ϵ. The MCP's energy losses due to the e^+e^- pair production can be written as

$$\left(-\frac{dE_\chi}{dx}\right)_{e^+e^-\text{pair}} = n\int_{2m_e}^{E_\chi - m_\chi} d\omega \frac{d\sigma_{e^+e^-\text{pair}}}{d\omega}\omega, \tag{7}$$

where $\omega = E_{e^+} + E_{e^-}$ is the total energy of e^+e^- pair. The cross section $d\sigma_{e^+e^-}/d\omega$ can be taken [56] in the ultrarelativistic approximation, when the energies of initial and final MCPs are high, $E'_\chi, E_\chi \gg m_\chi, m_e$, as well as the energies of electron and positron, $E_{e^+}, E_{e^-} \gg m_e$. In particular, the integration over the energy of positron yields the spectrum of the produced pair,

$$\frac{d\sigma_{e^+e^-\text{pair}}}{d\omega} = \int_{m_e}^{\omega - m_e} \frac{d\sigma_{e^+e^-\text{pair}}}{dE_{e^+} dE_{e^-}} dE_{e^+},$$

where the double differential cross section is written as

$$\frac{d\sigma_{e^+e^-\text{pair}}}{dE_{e^+} dE_{e^-}} = Z^2 \epsilon^2 \frac{\alpha^2 r_e^2}{2\pi} \frac{E'_\chi - \omega}{\omega^2 E_\chi} G, \tag{8}$$

and the value of G is given in Appendix A.

In the given material, the energy losses of all the types depend on the MCP energy E_χ, mass m_χ, and parameter ϵ. We illustrate their impacts with plots of Fig. 2. We observe that in different parts of the model parameter space, different mechanisms dominate at a given energy. In particular, one can neglect the ionization energy loss of the MCP at energies $E_\chi \gtrsim 10$ GeV.

The energy loss of the MCP on its way from the production point through the media to the detector can significantly reduce its energy. It should be taken into account when estimating the energy release in the detector due to the MCP elastic scattering inside the detector, which provides the MCP signal signature. In the case of large energy loss, the MCP energy may drop below the threshold accepted for the energy release to be observable. Such a low-energy MCP avoids detection.

D. Multiple scattering

We should also take into account the deflection of the MCP trajectory from the rectilinear one, which happens mostly due to multiple elastic scatterings off nuclei and electrons in the media; see the corresponding Feynman diagrams in Figs. 1(a1) and 1(a2). For the nucleus case, the averaged squared deflection angle of the MCP per unit propagation length reads

$$\frac{d\bar{\theta}^2_{\chi Z}}{dx} = n \int_0^\pi d\theta_\chi \theta_\chi^2 \frac{d\sigma_{\chi Z}}{d\theta_\chi}, \tag{9}$$

with the scattering cross section on a nucleus,

$$\frac{d\sigma_{\chi Z}}{d\theta_\chi} = \frac{Z^2 \epsilon^2 r_e^2 m_e^2}{4 E_\chi^2 \beta_\chi^2} \frac{1 - \beta_\chi^2 \sin^2(\frac{\theta_\chi}{2})}{\sin^2(\frac{\theta_\chi}{2}) + 1/(2a p_\chi)^2} 2\pi \sin\theta_\chi, \tag{10}$$

where $a \simeq 111 Z^{-1/3}/m_e$ is the screening parameter for the Thomas-Fermi atoms.

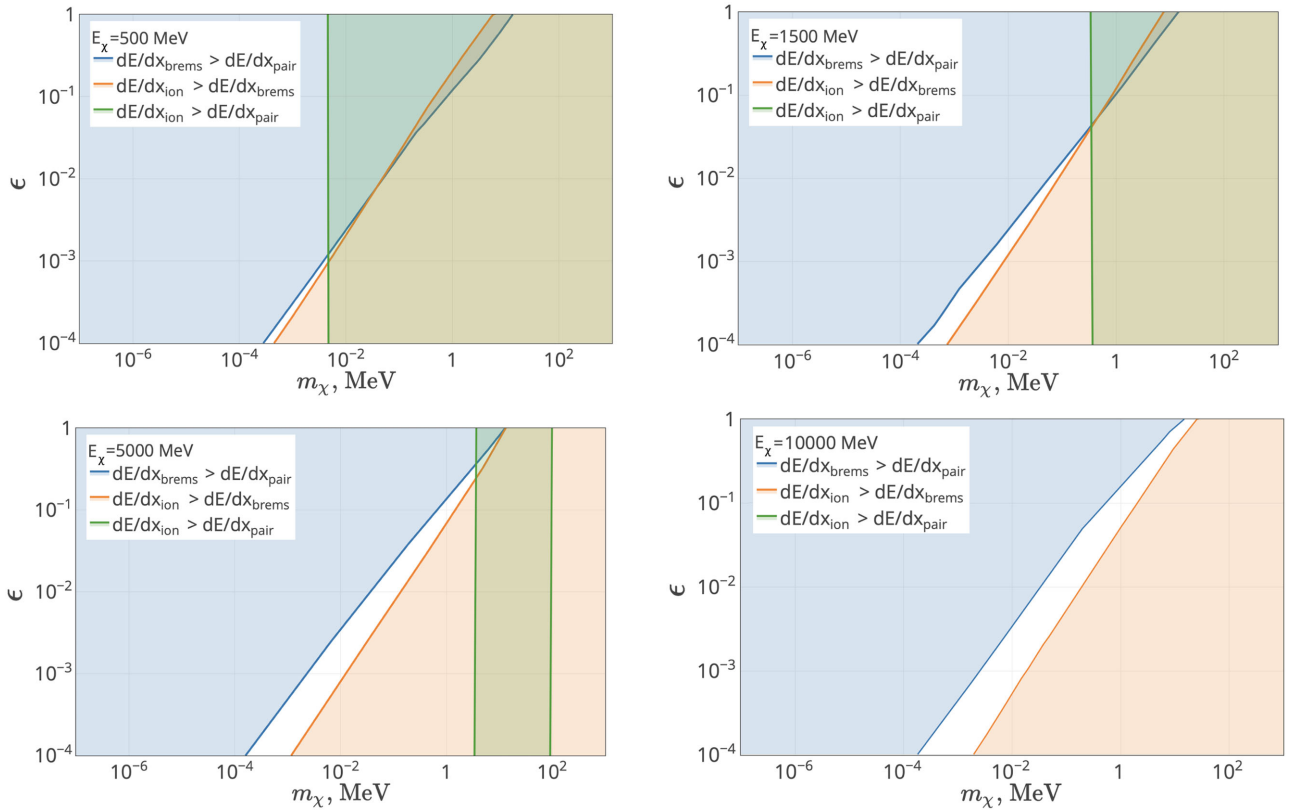

FIG. 2. The diagrams showing in which parts of the model parameter space which mechanism of the energy loss dominates. There are four plots for MCP energies $E_\chi = 500$ MeV, $E_\chi = 1.5$ GeV, $E_\chi = 5$ GeV, $E_\chi = 10$ GeV.

Similarly, for the case of MCP deflection by the atomic electron, one has the following expression for the average squared angle per unit propagation length:

$$\frac{d\overline{\theta^2_{\chi e}}}{dx} = Z\frac{N_A\rho}{M_A}\int_0^\pi \theta_\chi^2 \frac{d\sigma_{\chi e}}{d\theta_\chi} d\theta_\chi \Theta(E_\chi - E'_\chi - \alpha^2 m_e/2), \quad (11)$$

where the differential cross section in the laboratory frame is

$$\frac{d\sigma_{\chi e}}{d\theta_\chi} = \frac{2}{\pi}\sin\theta_\chi \frac{\epsilon^2 r_e^2 m_e |\vec{p}_\chi{}'|}{E'_e|\vec{p}_\chi|} \times \frac{m_e^2(E_\chi^2 + E_\chi'^2) + \frac{1}{2}(m_e^2 + m_\chi^2)(2m_\chi^2 - 2(p_\chi p_{\chi'}))}{(2m_\chi^2 - 2(p_\chi p_{\chi'}))^2}. \quad (12)$$

The last term in Eq. (11) is the step function, which accounts for screening effects. In particular, the additional condition should be imposed on the MCP transfer momentum squared, $-t = -(p'_\chi - p_\chi)^2 \gtrsim 1/R^2_{\rm scr}$, where $R_{\rm scr} \simeq (\alpha m_e)^{-1}$ is the typical screening radius for the atomic electrons. The latter condition implies the following inequality: $E'_\chi \lesssim E_\chi - \frac{\alpha^2}{2} m_e$, which defines the step function $\Theta(x)$ in the integral of (11). It refers to the fact that the energy of the initial electron is below its mass because of the binding energy $-\alpha^2 m_e/2$.

III. REVISITING SLACMQ BOUNDS ON MCPS

In this section, we revise the SLACmQ bounds on MCPs using detailed information on the expected MCP spectra and geometry of the SLACmQ experiment provided in Ref. [54].

In particular, we reconsider the limits associated with MCP stopping power, time resolution, and angular acceptance of the SLAC detector. The revised constraints we obtain in this way are similar to the ones from Ref. [54].

A. Stopping power

Let us consider first the impact of stopping power on bounds on MCP parameter space obtained by the SLACmQ experiment; see its layout in Fig. 3. The SLACmQ collected data of 3.8×10^{18} EOT. It employed a pulsed beam of 29.5 GeV electrons hitting the target made mostly of rhenium (25%) and tungsten (75%). On the way to the detector, placed at the distance $S = 110.1$ m from the target, MCPs passed downstream through sandstone, with an effective density $\rho = 2.19$ g/cm^3 and a length of $L \simeq 88.5$ m. Note that MCPs are produced in the target mainly due to the bremsstrahlung process, $eN \to eN\chi\overline{\chi}$, which implies that the production cross section scales as $\propto \alpha^4\epsilon^2 Z^2$. Therefore, the number of produced MCP pairs is proportional to $N_{\rm prod} \propto \epsilon^2$.

The predominant signature of the MCP used for detection is its elastic scattering off electrons in the far detector, $\chi e^- \to \chi e^-$; see the corresponding diagrams in Fig. 1(a1). Hence, assuming $\epsilon \ll 1$ and MCP reach the detector, the part of MCPs which hit the electrons on the way through the detector scales as $N_{\rm det} \propto \epsilon^2$. In addition, we note that for $\epsilon \ll 1$ and $m_\chi \gg m_e$, both the rate of MCP production and their attenuation rate are small. Therefore, as long as the attenuation rate of MCP is negligible, the number of expected signal events scales as $N_{\rm sig} \propto \epsilon^4$. To set the constraints at a given confidence level (typically 90% C.L. or 95% C.L.) in that region of MCP's parameter space, one should set $s_{\rm up} \simeq N_{\rm sig}$, where $s_{\rm up}$ is the upper limit on the average number of signal events for the given sum of signal and background events. In Fig. 6, these bounds correspond to the lower edge of the SLACmQ [54] excluded contour. We adopt that curve from Fig. 5.17 of Ref. [54]. It differs noticeably from the curve presented in the seminal work [53] as the upper limits of SLACmQ on the parameter ϵ.

Let us consider the attenuation of the MCP initial energy flow I_0,

$$I = I_0 \exp\left(-\frac{L}{X_\chi}\right),$$

where X_χ is the MCP attenuation length and L is the distance traveled by the MCP in matter. In case of the SLACmQ experiment, the MCP attenuation length can be estimated as follows:

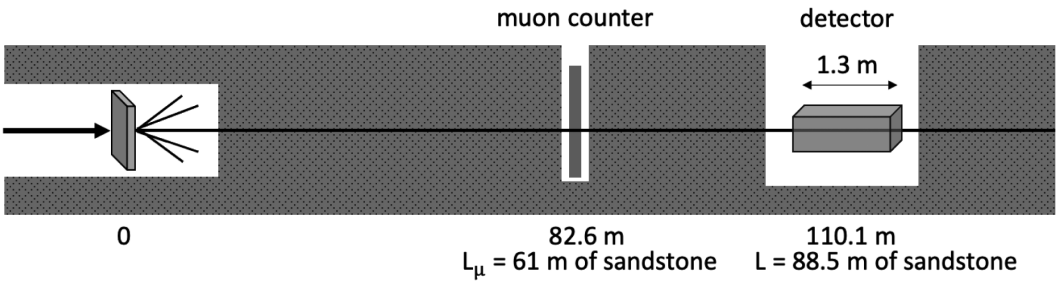

FIG. 3. Layout of SLACmQ experiment.

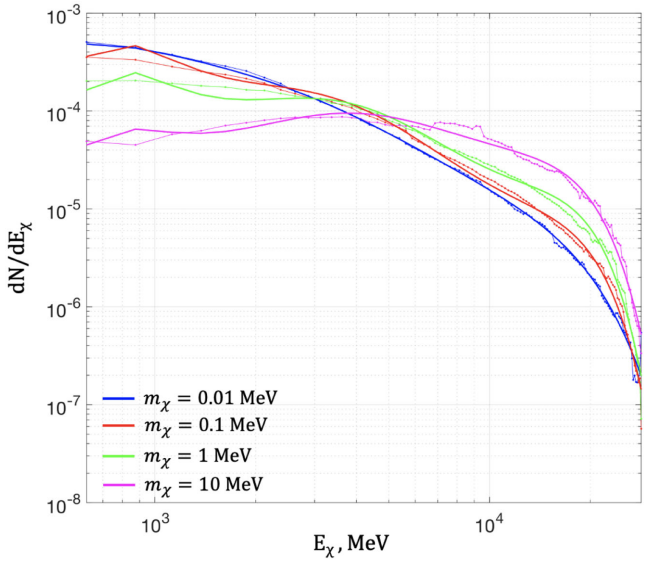

FIG. 4. Approximations to the differential energy spectra from SLACmQ data [54] normalized to inity for a set of MCP masses m_χ and $\epsilon = 10^{-3}$.

$$X_\chi = \int_{E_{\min}}^{E_{\max}} dE_\chi \frac{1}{N}\frac{dN}{dE_\chi} \int_{E_{\rm cut}^\chi}^{E_\chi} \frac{dE'_\chi}{|dE'_\chi/dx|}, \tag{13}$$

where E_χ is initial energy of MCP, $E_{\rm cut}^\chi$ is the energy threshold of MCP detection in the experiment, $E_{\min} = 0.125$ GeV, and $E_{\max} = 29.5$ GeV is the beam energy [54]. The total energy losses are

$$\left(\frac{dE_\chi}{dx}\right)_{\rm tot} = \left(\frac{dE_\chi}{dx}\right)_{\rm ion} + \left(\frac{dE_\chi}{dx}\right)_{\rm rad} + \left(\frac{dE_\chi}{dx}\right)_{\rm pair}. \tag{14}$$

The normalized to unity spectra $N^{-1}dN/dE_\chi$ of the produced MCP are taken from Table A. 2 in the Appendix of [54]; in Fig. 4, we show them for various masses m_χ.

The account of attenuation of the MCP passing through the matter changes the upper bound on ϵ at a given mass m_χ as follows:

$$\epsilon^4 = \epsilon^4_{\rm u.b.} \exp\left(-\frac{L}{X_\chi(\epsilon_{\rm u.b.})}\right), \tag{15}$$

where ϵ is the charge value of the MCPs that would reach the detector without energy loss (so that $s_{\rm up} \propto \epsilon^4$), and $\epsilon_{\rm u.b.}$ is the maximum charge value of the MCP that reach the detector with the proper accounting of their energy losses.

We note that for the relatively large charge, $\epsilon \gtrsim 10^{-2}$–10^{-1}, and $m_\chi \gtrsim m_e$ the rate of MCP production is fairly high. On the other hand, the rate of MCP absorption in the dump due to ionization and e^+e^- pair production is also high. Thus, the number of produced MCP is compensated by their attenuation in the dump. Moreover, numerical calculations reveal that for $\epsilon \ll 1$ and $m_\chi \lesssim m_e$ the radiation stopping power of MCP is not negligible and plays the dominant role in their absorption in the dump. In Fig. 5, the typical stopping power and its impact on the limit is illustrated for $X_\chi \simeq L$ and two values of MCP energy at production, which are relevant for the SLACmQ experiment.

B. Angular and timing acceptance

There are also two important benchmark conditions that should be taken into account to constrain the charge-mass parameter space of MCP in the case of SLACmQ. The first one is associated with the time interval of data taking. The arrival time of the MCPs in the detector is defined by the

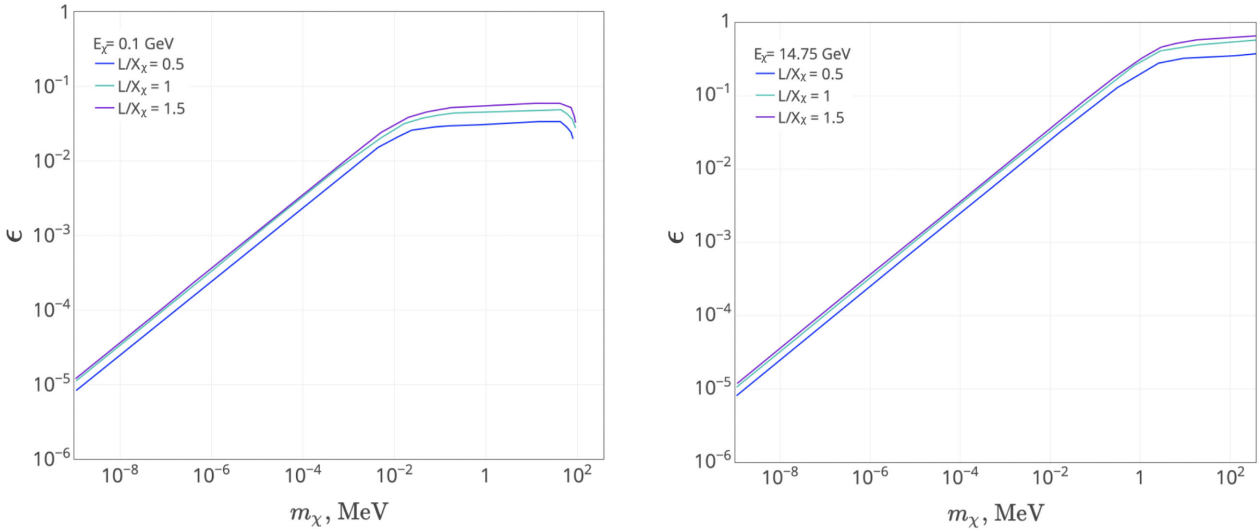

FIG. 5. Illustration of the stopping power for two examples of MCP initial energies.

muon beam scintillating counters located between the target and the detector at the distance of $S_\mu = 82.6$ m from the target ($L_\mu = 61$ m through sandstone) as shown in Fig. 3. The data are collected during the time interval $\Delta t_{\rm coll} = 250$ ns. The offset of synchronized signal is such that the muon signals came to muon counters in $\Delta t_{\rm off} = 60$ ns after the start of main timing window. It is assumed that the muons are (ultra)relativistic and collisionless; hence they reach the muon counter without any delay with respect to the light. Indeed, the typical radiation length of the muon can be estimated as $X_0^\mu \simeq X_0^e (m_\mu/m_e)^2 \simeq 4.4 \times 10^4 X_0^e$, for $X_0^e \simeq \mathcal{O}(1)$ cm that implies $X_0^\mu \simeq 440$ m, so that muon loses a small amount of the initial energy when it reaches the detector at the typical distance of 110 m. On the other hand, the produced in the target MCP of energy E_i can scatter off the sand and reach the muon counter with time delay of

$$\Delta\tau_\mu = \int_{S_\mu}^{0} dx \frac{1-\beta}{\beta} = \int_{E_i}^{E_\mu} \frac{dE}{|dE/dx|}\frac{1-\beta}{\beta}, \tag{16}$$

where E_μ is the MCP energy when it enters the muon counter, and the MCP velocity is $\beta \equiv \sqrt{1 - m_\chi^2/E^2}$. Then, the MCP has a time slot of

$$\Delta\tau_\chi \equiv \Delta t_{\rm coll} - \Delta t_{\rm off} - \Delta\tau_\mu$$

to reach the detector while the time window for the data collection is still open. Therefore, the MCP must cover the distance $L - S = L_\mu - S_\mu = 27.5$ m in a shorter time. This traveling through the sandstone is also accompanied by additional time delay due to scattering. This energy loss makes MCP less relativistic. Taking this into account, we obtain the following condition for MCP to arrive in time and be recorded:

$$\int_{L_\mu}^{L} \frac{dx}{\beta c} = \int_{E_L}^{E_\mu} \frac{dE}{|dE/dx|}\frac{1}{\beta} < \Delta\tau_\chi, \tag{17}$$

where E_L is the MCP energy in the detector.

If the energy losses are small, the energies of MCP in front of the scintillating counters are $E_L \approx E - |\frac{dE}{dx}|L$, $E_\mu \approx E - |\frac{dE}{dx}|L_\mu$; if not, it is necessary to solve the equation,

$$\int_{E_L}^{E} \frac{dE}{|dE/dx|} = L,$$

where dE/dx is from Eq. (14) and takes into account the energy loss in matter. To solve this equation, we adopt the approximate expressions from Appendix B. It must be pointed out that such time arriving constraints were not taken into account in the original paper [54].

The second benchmark condition is associated with the detector angular acceptance of 2 mr. We estimate the multiple scattering angle of MCP as a function of energy it has in front of the detector (E_L) by using Eqs. (9) and (11) and require it to be

$$\theta_\chi = \sqrt{\overline{\theta_Z^2} + \overline{\theta_e^2}} < 2 \text{ mr}. \tag{18}$$

C. Revised exclusion plot

We have explained previously, all the steps towards reevaluation of the SLACmQ bounds on models with MCP. All of the numerical calculations we perform with the approximate spectrum of MCP presented in Ref. [54]. In Fig. 6, we show the resulted exclusion region in the (m_χ, ϵ_χ) plane, which is determined by Eqs. (15), (17), and (18). As expected, the MCP scatterings are mostly important for relatively large charges and small masses. Most critical are deflections of the MCP trajectories depicted by the green dotted line.

The upper limit obtained in this way is similar to the one presented in Ref. [54], which corresponds to the upper edge curve in Fig. 5.17 of Ref. [54]. As one can see from Fig. 6,

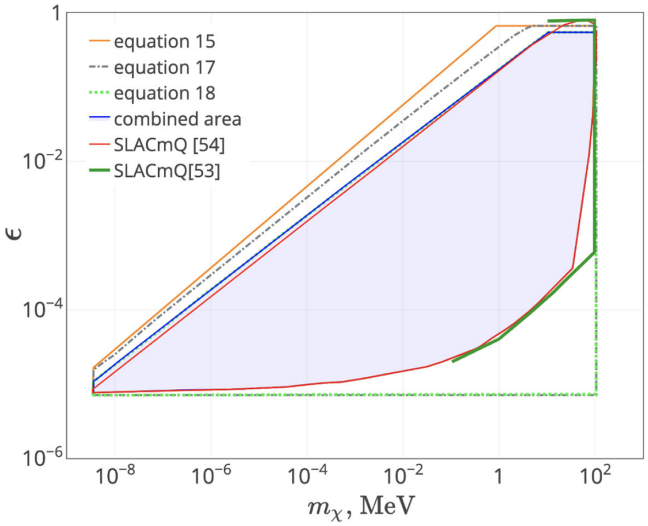

FIG. 6. Regions bounded from Eqs. (15), (17), and (18) and the combined exclusion region from our analysis of the SLACmQ data (*shaded blue region*). In particular, *the orange solid line* is the numerical solution $\epsilon_{\rm u.b.}$ to Eq. (15), for which ϵ is the charge fraction of the MCP that would reach the SLAC detector without energy loss; the latter ϵ is adapted from lower edge curve in Fig. 5.17 of Ref. [54] (see text for details). The *grey dash-dotted line* is the solution to Eq. (17) that is associated with time arriving constraints. The *green dotted line* is the solution to Eq. (18) that is associated with MCP multiple scattering constraints. The obtained region closely matches the result of Ref. [54] (*red solid line*) and refines that published in the original SLACmQ paper [53] (*green solid line*).

the exclusion region from the original publication [53] of the SLACmQ Collaboration is rather limited in mass and has no upper bounds. What is more important, there is a triangular region at $\epsilon \sim 10^{-3}$ and $m_\chi \sim 100$ MeV, which we find not constrained from the SLACmQ data, contrary to their publication.[1] This region is also open in Ref. [54]. It is worth mentioning again that we adopt the lower edge of the curve SLACmQ [54] shown in Fig. 6 from Fig. 5.17 of the Ref. [54]. The adopted in this way numerical values of the regarding coupling correspond to the ϵ in Eq. (15).

IV. CALCULATION OF THE DOUBLE-DIFFERENTIAL CROSS SECTION OF MCP PAIR PRODUCTION

In this section, we describe our procedure of calculation the double-differential cross section of MCP production in electron scattering off nucleus. At the sufficiently small MCP charge, the production happens mostly through emission of the virtual photon,

$$e(p_1)N(\mathcal{P}_2) \to e(p_3)\gamma^*(p_{\chi_1}+p_{\chi_2})N(\mathcal{P}_4) \to \\ \to e(p_3)\chi(p_{\chi_1})\bar{\chi}(p_{\chi_2})N(\mathcal{P}_4), \tag{19}$$

and since it is purely electromagnetic process, we calculate it in the exact tree-level approach. The Feynman diagrams referring to the tree-level amplitude are presented in Fig. 7. This contribution is linear in ϵ, and we neglect contributions proportional to ϵ^2 coming from other diagrams.

The NA64e experiment utilizes the electron beam of $E_1 = 100$ GeV and lead target (see below Sec. V). We carry out the integration of squared exact tree-level amplitude over the phase space of the process (19) by exploiting the latest version of the `CalcHEP` package [57]. The vertex for $NN\gamma$ interaction we take to be

$$ieZF(-q^2)\gamma_\mu. \tag{20}$$

It corresponds to the spin-1/2 nucleus interaction with a photon; here, $q = (\mathcal{P}_2 - \mathcal{P}_4)$ is the nucleus transfer momentum, and $\mathcal{P}_2$ and $\mathcal{P}_4$ are the initial and final momenta of the nucleus. The elastic form factor $F(-q^2)$ has the following form:

$$F(t) = \frac{a^2 t}{(1+a^2 t)}\frac{1}{(1+t/d)}, \tag{21}$$

where $t = -q^2$ is the squared transfer momentum, $a = 111Z^{-1/3}/m_e$ and $d = 0.164A^{-2/3}$ GeV^2 are screening and nucleus parameters, respectively. For the lead active target (atomic number $A = 207$, nuclear charge $Z = 82$) of the NA64e, one estimates the following typical momenta

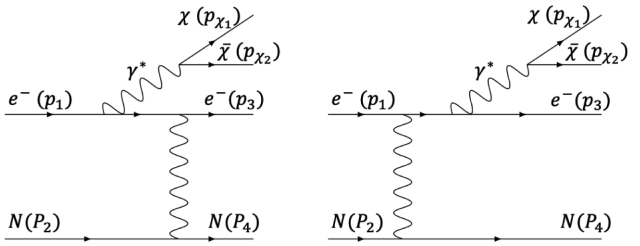

FIG. 7. Leading Feynman diagrams for MCP pair production process.

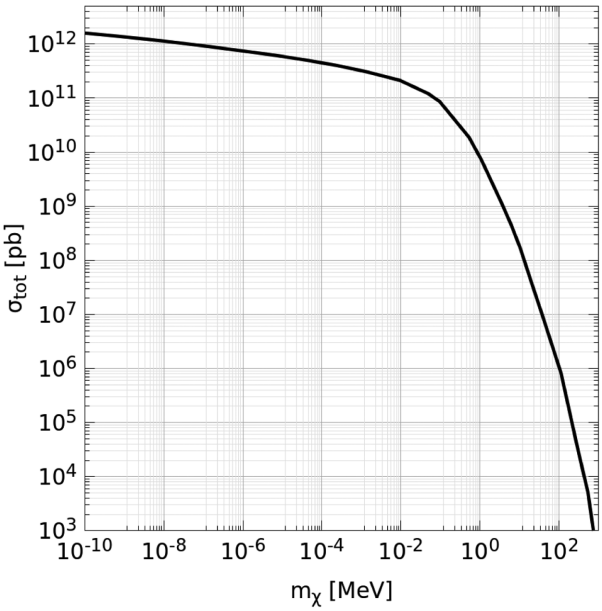

FIG. 8. Total cross section of MCP pair production as the function of m_χ for $E_{\text{beam}} = 100$ GeV and $\epsilon = 1$.

transfer associated with screening effects and nucleus size respectively: $\sqrt{t_a} = 1/a \simeq 2 \times 10^{-5}$ GeV and $\sqrt{t_d} = \sqrt{d} \simeq 6.7 \times 10^{-2}$ GeV.

We implement the form factor (20), (21) in the C++ code of `CalcHEP` and carry out `VEGAS` Monte Carlo integration of the cross section for various masses m_χ in order to obtain the differential energy spectra of the produced MCP. Before presenting its form, let us note that to check our calculations, we integrate the double-differential cross section over the MCP energies and thus, evaluate the total MCP production cross section, which is shown in Fig. 8 as a function of MCP mass m_χ. A similar plot can be found in Fig. 3 of Ref. [58], where the calculation is done in the limit of massless electron and for $m_\chi > 1$ MeV. We have checked that in this limit our estimate of the total cross section matches with that of Ref. [58] with the accuracy of a few percent.[2] Therefore, in our study, we extend the

[1]We thank A. Prinz and J. Jaros for helping us to clarify this discrepancy in private correspondence.

[2]We thank J. Pradler, X. Chu and A. Pukhov for helping us to do this cross-check.

previous work on (much) lighter MCP and account corrections due to nonzero electron mass.

V. SENSITIVITY OF THE NA64*e*

Before evaluating the MCP search sensitivity with the NA64*e* experiment, let us briefly describe its main features relevant for further discussion. The NA64*e* detector is schematically shown in Fig. 9. The experiment employed the optimized H4 100 GeV electron beam from the CERN SPS. The beam has a maximal intensity $\simeq 10^7$ electrons per SPS spill of 4.8 s produced by the primary 400 GeV proton beam with an intensity of few 10^{12} protons on target. The detector utilized the beam defining scintillator (Sc) counters S_{1-4} and veto $V_{1,2}$, a magnetic spectrometer consisting of two successive dipole magnets$_{1,2}$ with the integral magnetic field of $\simeq 7$ T $\cdot$ m and a low-material-budget tracker. The tracker was a set of two upstream micromegas chambers $T_{1,2}$, and two downstream $MM_{3,4}$, allowing the measurements of e^- momenta with the precision $\delta p/p \simeq 1\%$. To significantly improve the electron identification, the synchrotron radiation (SR) emitted in the magnetic field of the magnets$_{1,2}$ was used for their tagging with a SR detector (SRD) [59,60]. By using this method, the initial fraction of the hadrons in the beam $\pi/e^- \lesssim 10^{-2}$ was further suppressed by a factor $\simeq 10^3$. The detector was also equipped with an active target, which is an electromagnetic calorimeter (ECAL), a matrix of 6×6 Shashlik-type counters assembled from lead and scintillator plates for measurement of the electron energy $E_{\rm ECAL}$. Each counter has $\simeq 40$ radiation lengths (X_0) with the first $4X_0$ serving as a preshower detector. Downstream of the ECAL, the detector was equipped with a large high-efficiency veto counter VETO, and a massive, hermetic hadronic calorimeter (HCAL) of $\simeq 30$ nuclear interaction lengths in total. The modules $HCAL_{1-3}$ provided an efficient veto to detect muons or hadronic secondaries produced in the e^-A interactions in the target. The search described in this paper uses the data sample of $N_{\rm EOT} = 2.84 \times 10^{11}$ EOT collected in the three years 2016, 2017, and 2018. The method, briefly discussed in Sec. I and proposed in Refs. [59], is based on the detection of the missing energy, carried away by the hard bremsstrahlung MCPs produced in the process $e^-N \to e^-N\gamma^*(\to \bar{\chi}\chi)$ of high-energy electrons scattering in the active ECAL target. The advantage of the NA64 idea compared to the beam dump one is that its sensitivity is proportional to ϵ^2. The latter is associated with the χ production and its subsequent prompt escaping the detector without interactions in the HCAL modules.

In the following, similar to Ref. [58], we first calculate the number of missing energy events associated with MCP emission by energetic electrons incident on the thin target. The latter implies a single scattering on average and then a rapid degradation of the electron energy due to bremsstrahlung. For the case of the NA64*e*, we assume that the incident electron produces MCP in the first scattering within the first radiation length of the ECAL target of the NA64*e*, $X_0 \simeq 0.56$ cm. This assumption is justified by the fact that the high energy electron loses most of its energy in a single process transferring it to the emitted photon.

Now let us evaluate the sensitivity of the NA64*e* to model parameters of MCP taking into account the energy loss of the millicharged particles in the detector. This energy transfers to the electromagnetic channel which NA64*e* closely monitors and hence, sums up with all other sources of electromagnetic activity. The experimental signature of the MCP detection would be an event with the missing energy $E_{\rm miss} \gtrsim 50$ GeV; see, e.g., Ref. [61]. The events with lower missing energy are not considered as potentially signal events. Therefore, the estimate of MCP energy loss within the detector is an important step towards understanding prospects of the NA64*e* in testing models with MCP.

The total number of MCP pairs produced in the process $eN \to eN\chi\bar{\chi}$ can be calculated as follows:

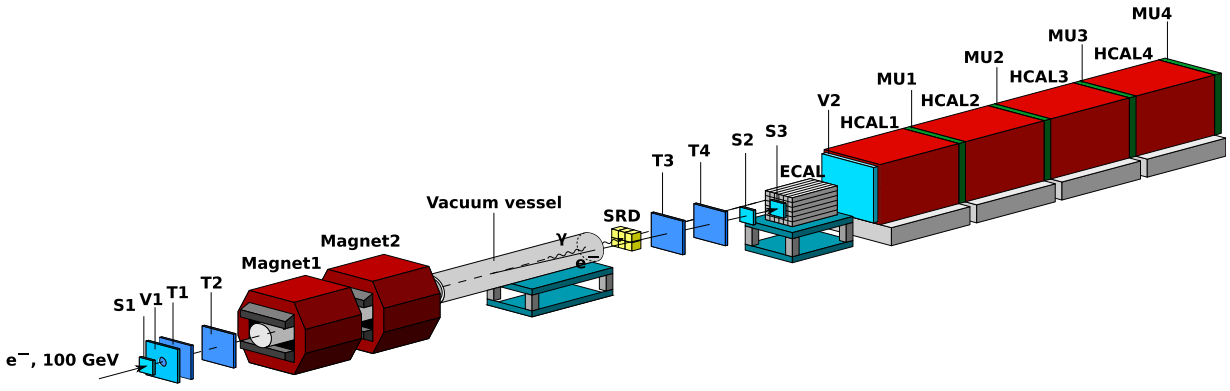

FIG. 9. Schematic illustration of the setup to search for MCP production in the reaction $e^-N \to e^-N\gamma^*(\to \bar{\chi}\chi)$ of 100 GeV e^- incident on the active ECAL target. See text.

$$N_{\chi\bar{\chi}} = \frac{\rho N_A}{M_A} N_{\rm EOT} X_0 \int_{\rm s.b.} dE_{\chi_1} dE_{\chi_2} \frac{d\sigma(E_{\rm beam})}{dE_{\chi_1} dE_{\chi_2}}. \quad (22)$$

Here, $N_{\rm EOT}$ is a number of electrons accumulated on target, $\rho = 11.34\ {\rm g\,cm^{-3}}$ is a density of the lead ECAL active target, $M_A = 207\ {\rm g\,mol^{-1}}$ is the atomic mass of the target, N_A is Avogadro's number, $E_{\rm beam} = 100$ GeV is the energy of initial electron from the beam, and the double-differential cross section of $\chi\bar{\chi}$ production $d\sigma/(dE_{\chi_1} dE_{\chi_2})$ is calculated by using `CalcHEP` as described in Sec. IV. The diplots corresponding to several choices of MCP mass are presented in Fig. 10. Naturally, the distribution is symmetric with respect to the interchange of the positive and negative MCP.

The integration over E_{χ_1} and E_{χ_2} in (22) is performed inside the signal box (s. b.). This region is determined by the missing energy cut of the electromagnetic calorimeter (ECAL) exploited in NA64e, $E^{\rm th}_{\rm miss} \equiv 50$ GeV, and the initial energy of the electron beam $E_{\rm beam} = 100$ GeV as follows:

$$E^{\rm th}_{\rm miss} \lesssim E_{\chi_1} + E_{\chi_2} - \Delta E_{\chi_1} - \Delta E_{\chi_2} \lesssim E_{\rm beam}. \quad (23)$$

Here, E_{χ_1} and E_{χ_2} are the MCP energies at production, and ΔE_{χ_1} and ΔE_{χ_2} are the total energy depositions of the millicharged particles in the ECAL due to possible electromagnetic rescattering on their way out. These quantities are estimated through the differential energy loss as follows:

$$\Delta E_{\chi_{1,2}} = -\int_0^{L_T} \frac{dE_{\chi_{1,2}}}{dx} dx = E_{\chi_{1,2}}(0) - E_{\chi_{1,2}}(L_T) \geq 0,$$

and the integral goes over the effective width of the lead material in ECAL, $L_T = 22.5$ cm. The MCP energies at the exit from ECAL $E_{\chi_{1,2}}(L_T)$ can be expressed through the energy of MCP at production $E_{\chi_{1,2}}(0) = E_{\chi_{1,2}}$ by solving the equation,

$$\int_{E_{\chi_{1,2}}(0)}^{E_{\chi_{1,2}}(L_T)} dE_{\chi_{1,2}} \frac{1}{(dE_{\chi_{1,2}}/dx)} = -L_T, \quad (24)$$

where for $(dE_{\chi_{1,2}}/dx)$, we use numerical approximations collected in Appendix A. Finally, for the given energies of MCP at production in the target, $E_{\chi_{1,2}}(0)$, one has the following region for the signal box:

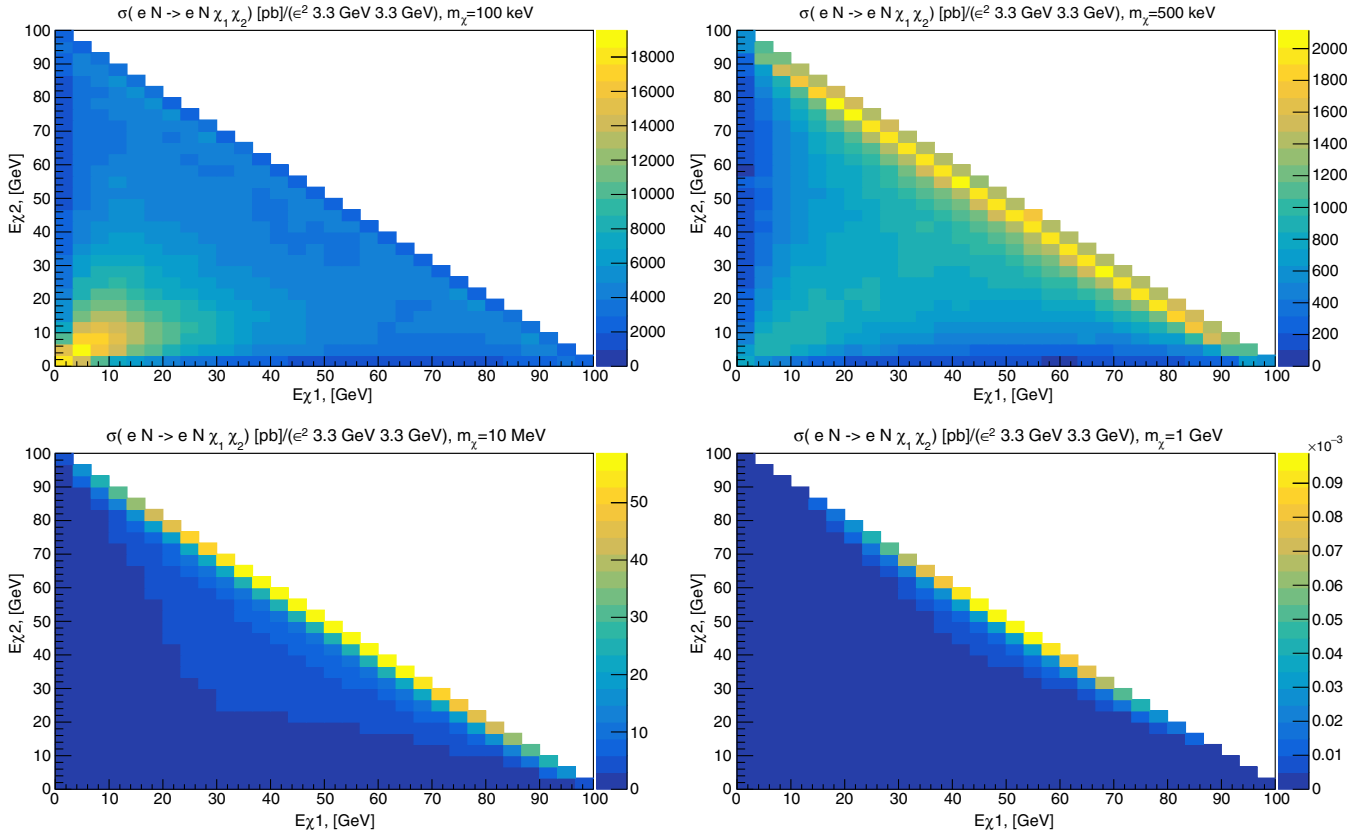

FIG. 10. Double-differential cross section of the MCP pair production as a function of MCP energies E_{χ_1} and E_{χ_2} for a set of MCP masses m_χ and energy of incident electron $E_{\rm beam} = 100$ GeV. Note that only events above the line $E_{\chi_1} + E_{\chi_2} > 50$ GeV are interesting with cuts adopted in NA64e experiment.

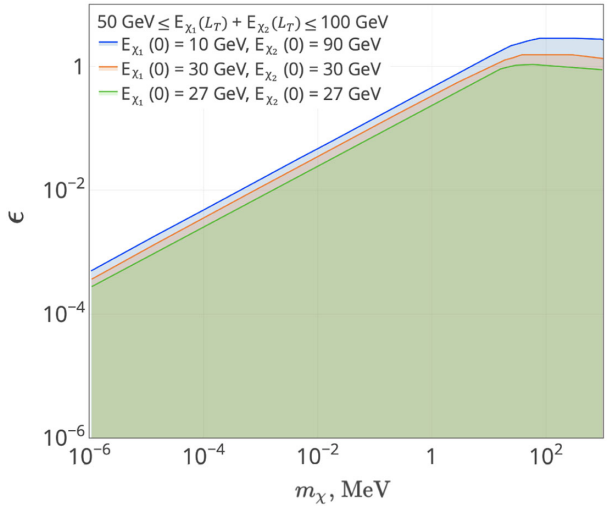

FIG. 11. The MCP pairs with a chosen initial energies do not contribute to the signal events for parameters above the corresponding lines.

$$E_{\rm miss}^{\rm th} \lesssim E_{\chi_1}(L_T) + E_{\chi_2}(L_T) \lesssim E_{\rm beam}. \tag{25}$$

The relevance of the energy transfer to the electromagnetic cascade is demonstrated in Fig. 11. There we chose three examples of MCP pairs with total energy exceeding the threshold value in NA64e. In the regions above the corresponding lines, the MCP loses its energies emitting energetic photons, which are collected by the NA64e ECAL. Finally, the total MCP energy drops below the threshold, and so they do not contribute to the signal events.

Numerical calculations reveal that for the wide ranges of $\epsilon \lesssim 0.3$ and $m_\chi \lesssim 1$ MeV, the radiation energy loss of the millicharged particle (bremsstrahlung) dominates over the energy loss due to ionization, $\chi e \to \chi e$, and due to pair production, $\chi N \to \chi N e^+ e^-$. The energy loss of the millicharged particle due to the bremsstrahlung, $\chi N \to \chi N \gamma$, inside the Pb target can be approximated for the interesting energetic MCP as follows (see Appendix B):

$$\frac{1}{E_\chi}\frac{dE_\chi}{dx} \simeq -(X_0)^{-1}\epsilon^4\left(\frac{m_\chi}{m_e}\right)^{-2} \simeq -0.45\ \text{cm}^{-1}\epsilon^4\left(\frac{m_\chi}{1\ \text{MeV}}\right)^{-2}. \tag{26}$$

It helps to solve (24) for this region of the model parameter space. We note that for $\epsilon = 1$ and $m_\chi = m_e$, the result for the electron radiation length $X_0 \simeq 0.56$ cm is restored from Eq. (26). It implies the well-known result that the electron energy is reduced by factor of $e \simeq 2.71$ within the first radiation length in lead due to the radiation loss.

Estimated in this way, numbers of the signal events are outlined in Fig. 12 for a set of MCP masses and for the projected statistics of $N_{\rm EOT} = 5 \times 10^{12}$.

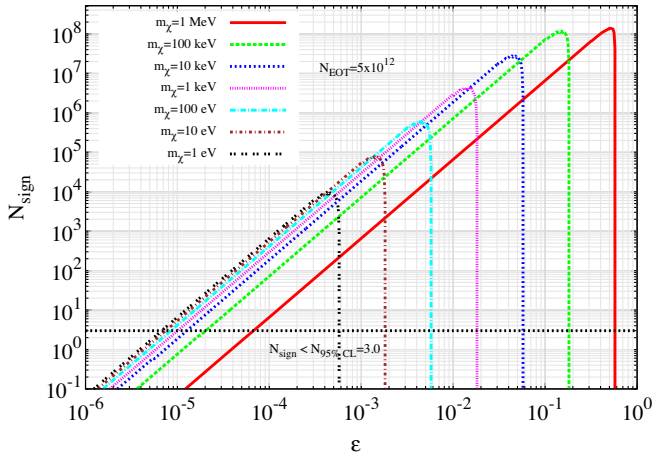

FIG. 12. Number of signal events $eN \to eN\gamma^*(\to \chi\bar{\chi})$ as function of ϵ.

We evaluate the lower 95% C.L. bound on the coupling ϵ by requiring $N_{\chi\bar{\chi}} > s_{\rm up} \equiv 3.0$, which in the Poisson statistics corresponds to the null result at zero background (that is a realistic assumption for NA64e and moderate number of incident electrons we utilize). The results are shown in Fig. 13 for the currently accumulated $N_{\rm EOT} = 2.84 \times 10^{11}$ and for the projected statistics $N_{\rm EOT} = 5 \times 10^{12}$ [62]. It is worth mentioning that magnetic field does not affect the sensitivity of the NA64e, since the

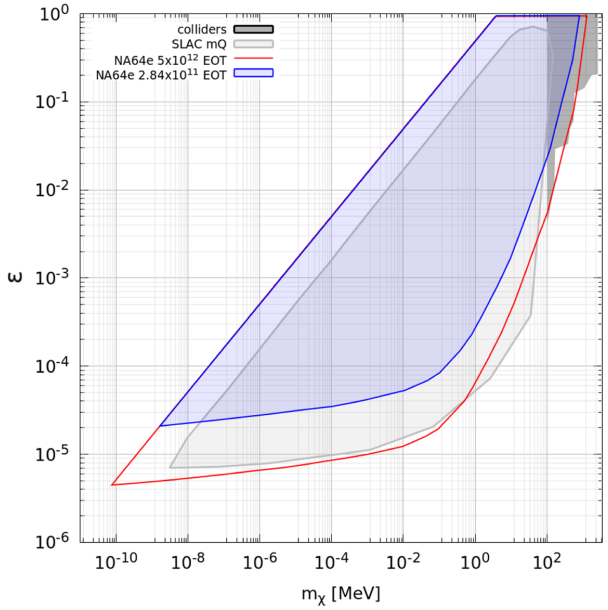

FIG. 13. Sensitivity contours (at 95% C.L.) of the NA64e in the (ϵ, m_χ) plane for the process $eN \to eN\gamma^*(\to \chi\bar{\chi})$. We account for nonzero electron mass in the calculation, $m_e \neq 0$, and suppose that MCP pairs are produced within the first layer (its width is about the electron radiation length) of the lead target. We also set $\alpha_{\rm QED} = 1/137$.

dominant part of MCPs is produced in the ECAL that is installed downstream after the magnetic spectrometers (see, e.g., Fig. 9). So that the magnetic field would not deflect the original direction of the MCP that can be potentially detected in the active target of the NA64e.

Concluding this section we note that it is worth to carry out a similar analysis for the MCP sensitivity of the muon fixed target experiments such as NA64μ and M^3 (see, e.g., Refs. [63–66]). In particular, the signal of muon missing energy events due to the MCP emission can be originated from the following process: $\mu N \to \mu N \chi\bar{\chi}$, for which the effects of the MCP passage through the detector should be taken into account. This task is beyond the scope of the present paper, and we leave it for future study.

VI. CONTRIBUTION OF VECTOR MESONS

In this section, we estimate a contribution of vector mesons, $V = \{\rho, \omega, \phi, J/\psi\}$, to MCP production at NA64e. We adopt the results of Ref. [67] to estimate the yield of vector mesons produced at NA64e in photonuclear reaction $\gamma N \to NV$ for the expected statistics $N_{\rm EOT} \simeq 5 \times 10^{12}$. The invisible branching ratio of mesons to MCP can be written as

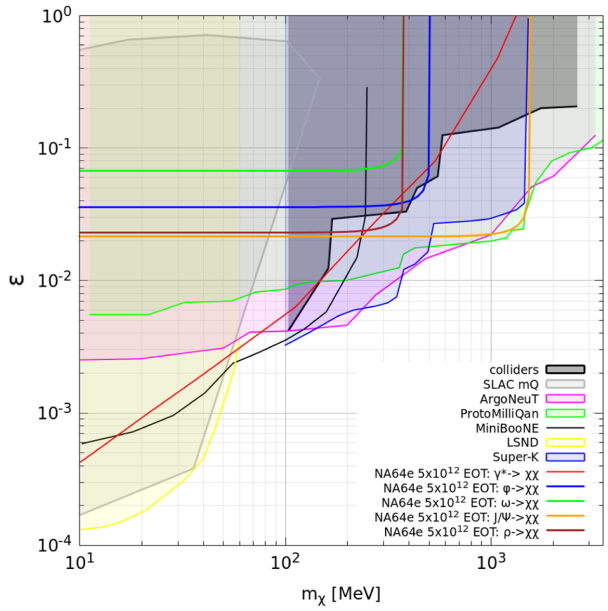

FIG. 14. The expected sensitivity of the NA64e in the (ϵ, m_χ) plane. We take into account invisible decays of vector mesons to the MCP, $V \to \chi\bar{\chi}$, and MCP production by the energetic beam electrons via bremsstrahlung-like mode $\gamma^* \to \chi\bar{\chi}$ for the prospect statistics $N_{\rm EOT} = 5 \times 10^{12}$ and MCP mass range 10 MeV $\leq m_\chi \leq 1.5$ GeV. The upper limits based on data of ArgoNeuT, LSND, Super-K, and ProtoMilliQan are taken from Ref. [68], while limits based on data of colliders and MiniBooNE are taken from Ref. [21]. SLACmQ limits are based on the present analysis. All constraints are set at 95% C.L.

$$\mathrm{Br}(V \to \chi\bar{\chi}) = \epsilon^2 \times \mathrm{Br}(V \to e^+e^-) \times (1 + 2m_\chi^2/m_V^2)(1 - 4m_\chi^2/m_V^2)^{1/2}. \quad (27)$$

In the absence of signal events, it implies the limit on ϵ for each meson mode, $V \to \chi\bar{\chi}$, of the following form:

$$\epsilon \gtrsim N_V^{-1/2} \cdot s_{\rm up}^{1/2} \cdot (\mathrm{Br}(V \to e^+e^-))^{-1/2} \times \quad (28)$$

$$\times (1 + 2m_\chi^2/m_V^2)^{-1/2}(1 - 4m_\chi^2/m_V^2)^{-1/4}. \quad (29)$$

Here, N_V denotes the total number of V mesons produced at NA64, which is taken from Table II of Ref. [67]. In Fig. 14, we show the corresponding limits in (ϵ, m_χ) plane.

VII. CONCLUSIONS

In the present paper, we investigate various effects associated with MCP passage through the matter. In particular, we discuss in detail the MCP energy losses in the matter due to the ionization, bremsstrahlung, and e^+e^- pair production. We also discuss the effects of the MCP trajectory deflection due to the multiple scattering in the matter. We implement these results to revise the bounds on the MCP parameters from SLACmQ experimental data. We find that our results are in a good agreement with the previous study [54]. Our study opens a part of the model parameter space previously considered as excluded on the base of published SLACmQ results [53].

In addition, by exploiting the state-of-the-art `CalcHEP` package, we calculate the exact tree-level cross section of the electron scattering off nucleus $e^-N \to e^-N\gamma^*(\to\chi\bar{\chi})$ to estimate the sensitivity of the NA64e fixed target experiment to MCP parameters. We find that the bremsstrahlung reaction, $\chi N \to \chi N\gamma$, is the dominant process of MCP energy losses in the detector of the NA64e for the parameter space of interest $\epsilon \lesssim 0.1$ and $m_\chi \lesssim 1$ MeV. To summarise, NA64e can test the models with MCP masses from about 10^{-4} eV to 1 GeV. In particular, we show that for the expected statistics of electrons incident on the target $N_{\rm EOT} \simeq 5 \times 10^{12}$ at NA64e, the relatively light MCP with $m_\chi \simeq 10^{-4}$ eV and $\epsilon \simeq 10^{-5}$ can be directly probed provided by the bremsstrahlung-like missing energy process $e^-N \to e^-N\gamma^*(\to\chi\bar{\chi})$, while the relatively large MCP with $m_\chi \simeq 1$ GeV and $\epsilon \simeq 2 \times 10^{-2}$ can be examined thanks to the invisible vector meson decay signature $eN \to eNJ/\psi(\to\chi\bar{\chi})$.

ACKNOWLEDGMENTS

We would like to thank R. Capdevilla, A. Celentano, X. Chu, P. Crivelli, S. Demidov, D. Forbes, Y. Kahn, M. Kirsanov, N. Krasnikov, G. Krnjaic, G. Lanfranchi, V. Lyubovitskij, L. Molina Bueno, J. Pradler, A. Prinz, A. Pukhov, G. Rubtsov, P. Satunin, P. Schuster, H. Sieber, F. Tkachov, and A. Zhevlakov for very helpful discussions and correspondences. The work on the estimate of the

expected sensitivity of the NA64e is partly supported by the Russian Science Foundation RSF Grant No. 21-12-00379. The work of N. A. on refining SLACmQ sensitivity was supported by the grant of the "BASIS" Foundation Grant No. 21-2-1-100-1.

APPENDIX A: FACTORS FOR THE SPECTRUM OF PAIR PRODUCTION

The function is defined by

$$G = -Ag\left(\frac{1}{1+\xi}\right) - B\xi\log\left(1+\frac{1}{\xi}\right) - \frac{C}{1+\xi} + \left(2\log\frac{E_{e^+}E_{e^-}}{2m_e\omega\sqrt{1+\xi}} - 1\right) \times \left(A\log\left(1+\frac{1}{\xi}\right) + B + \frac{C}{1+\xi}\right), \tag{A1}$$

where

$$A = \left(1-\frac{4}{3}\frac{E_{e^+}E_{e^-}}{\omega^2}\right)\left(1+\frac{\omega^2}{2E_\chi E'_\chi}\right) + \frac{4}{3}\xi\left(1-\frac{E_{e^+}E_{e^-}}{\omega^2}\right),$$

$$B = \frac{4}{3}\frac{E_{e^+}E_{e^-}}{\omega^2} - 1, \qquad C = -\frac{\xi}{3} - \frac{1}{6}\frac{\omega^2}{E_\chi E'_\chi} - \frac{1}{3}\frac{(E_{e^+}-E_{e^-})^2}{\omega^2},$$

$$\xi = \frac{m_\chi^2 E_{e^+}E_{e^-}}{4m_e^2 E_\chi(E_\chi-\omega)}, \qquad g(x) = -\int_0^x \log\frac{|1-t|}{t}\,dt,$$

and

$$\omega = E_{e^+} + E_{e^-}, \qquad E_\chi = E_{\chi'} + \omega.$$

APPENDIX B: NUMERICAL APPROXIMATIONS FOR THE ENERGY LOSS

This appendix presents the approximation formulae for the MCP energy loss due to bremsstrahlung and e^+e^- pair production. The bremsstrahlung energy losses can be approximated as

$$\left|\frac{dE_\chi}{dx}\right|_{\text{brems approx}} \approx 0.45\ \text{cm}^{-1} E_\chi \epsilon^4 \left(\frac{m_\chi}{1\ \text{MeV}}\right)^{-2}.$$

The MCP energy loss due to e^+e^- pair production can be described by different expressions for different ranges of MCP mass,

$$\left|\frac{dE_\chi}{dx}\right|_{e^+e^-\text{ pair approx}} = \tag{B1}$$

$$10^{-a_i}\epsilon^2\left(\frac{E_\chi}{1\ \text{MeV}}\right)^{d_i}\left(\frac{m_\chi}{1\ \text{MeV}}\right)^{c_i}[\text{MeV cm}^{-1}], \tag{B2}$$

where $e_{i-1} < \frac{m_\chi}{\text{MeV}} < e_i$, and $i = 1, \ldots, 5$, values of the coefficients are shown below: $e_0 = 0$,

$a_1 = 1.9281$	$c_1 = -0.0805$	$d_1 = 1.1340$	$e_1 = 2.154 \times 10^{-4}$
$a_2 = 2.3194$	$c_2 = -0.1964$	$d_2 = 1.1374$	$e_2 = 0.1551$
$a_3 = 2.7185$	$c_3 = -0.5705$	$d_3 = 1.1477$	$e_3 = 4.1596$
$a_4 = 2.6936$	$c_4 = -0.3986$	$d_4 = 1.1138$	$e_4 = 12.4520$
$a_5 = 2.8549$	$c_5 = 0.1423$	$d_5 = 1.0096$	$e_5 = 1 \times 10^3$

Recall in Sec. II that the ionization loss of MCP is negligible for the interesting energetic MCP, $E_\chi > 10$ GeV. Thus, the approximate overall energy loss of high energy MCP is given by the sum,

$$\left|\frac{dE_\chi}{dx}\right|_{\text{rad approx}} = \left|\frac{dE_\chi}{dx}\right|_{\text{brems approx}} + \left|\frac{dE_\chi}{dx}\right|_{e^+e^-\text{pair approx}}.$$

[1] A. Y. Ignatiev, V. A. Kuzmin, and M. E. Shaposhnikov, Is the electric charge conserved?, Phys. Lett. **84B**, 315 (1979).
[2] D. E. Brahm and L. J. Hall, U(1)-prime Dark matter, Phys. Rev. D **41**, 1067 (1990).
[3] M. Pospelov, A. Ritz, and M. B. Voloshin, Secluded WIMP dark matter, Phys. Lett. B **662**, 53 (2008).
[4] J. L. Feng, M. Kaplinghat, H. Tu, and H. B. Yu, Hidden charged dark matter, J. Cosmol. Astropart. Phys. 07 (2009) 004.
[5] J. M. Cline, Z. Liu, and W. Xue, Millicharged atomic dark matter, Phys. Rev. D **85**, 101302 (2012).
[6] S. Tulin, H. B. Yu, and K. M. Zurek, Resonant Dark Forces and Small Scale Structure, Phys. Rev. Lett. **110**, 111301 (2013).
[7] H. Liu, N. J. Outmezguine, D. Redigolo, and T. Volansky, Reviving millicharged dark matter for 21-cm cosmology, Phys. Rev. D **100**, 123011 (2019).
[8] C. Creque-Sarbinowski, L. Ji, E. D. Kovetz, and M. Kamionkowski, Direct millicharged dark matter cannot explain the EDGES signal, Phys. Rev. D **100**, 023528 (2019).
[9] R. Harnik, Z. Liu, and O. Palamara, Millicharged particles in liquid argon neutrino experiments, J. High Energy Phys. 07 (2019) 170.
[10] B. Holdom, Two U(1)'s and epsilon charge shifts, Phys. Lett. **166B**, 196 (1986).
[11] E. Izaguirre and I. Yavin, New window to millicharged particles at the LHC, Phys. Rev. D **92**, 035014 (2015).

[12] Z. Liu and Y. Zhang, Probing millicharge at BESIII via monophoton searches, Phys. Rev. D **99**, 015004 (2019).

[13] Y. Zhang, W. T. Zhang, M. Song, X. A. Pan, Z. M. Niu, and G. Li, Probing invisible decay of dark photon at BESIII and future STCF via monophoton searches, Phys. Rev. D **100**, 115016 (2019).

[14] Z. Liu, Y. H. Xu, and Y. Zhang, Probing dark matter particles at CEPC, J. High Energy Phys. 06 (2019) 009.

[15] J. Liang, Z. Liu, Y. Ma, and Y. Zhang, Millicharged particles at electron colliders, Phys. Rev. D **102**, 015002 (2020).

[16] Y. Bai, S. J. Lee, M. Son, and F. Ye, Muon g-2 from millicharged hidden confining sector, J. High Energy Phys. 11 (2021) 019.

[17] A. Ball, G. Beauregard, J. Brooke, C. Campagnari, M. Carrigan, M. Citron, J. De La Haye, A. De Roeck, Y. Elskens, R. E. Franco *et al.*, Search for millicharged particles in proton-proton collisions at $\sqrt{s} = 13$ TeV, Phys. Rev. D **102**, 032002 (2020).

[18] A. Ball *et al.* (milliQan Collaboration), Sensitivity to millicharged particles in future proton-proton collisions at the LHC with the milliQan detector, Phys. Rev. D **104**, 032002 (2021).

[19] J. Jaeckel, M. Jankowiak, and M. Spannowsky, LHC probes the hidden sector, Phys. Dark Universe **2**, 111 (2013).

[20] X. Chu, J. L. Kuo, and J. Pradler, Dark sector-photon interactions in proton-beam experiments, Phys. Rev. D **101**, 075035 (2020).

[21] K. J. Kelly and Y. D. Tsai, Proton fixed-target scintillation experiment to search for millicharged dark matter, Phys. Rev. D **100**, 015043 (2019).

[22] J. H. Kim, I. S. Hwang, and J. H. Yoo, Search for sub-millicharged particles at J-PARC, J. High Energy Phys. 05 (2021) 031.

[23] D. Gorbunov, I. Krasnov, Y. Kudenko, and S. Suvorov, Double-hit signature of millicharged particles in 3D segmented neutrino detector, Phys. Lett. B **822**, 136641 (2021).

[24] G. Marocco and S. Sarkar, Blast from the past: Constraints on the dark sector from the BEBC WA66 beam dump experiment, SciPost Phys. **10**, 043 (2021).

[25] G. Magill, R. Plestid, M. Pospelov, and Y. D. Tsai, Millicharged Particles in Neutrino Experiments, Phys. Rev. Lett. **122**, 071801 (2019).

[26] R. Acciarri *et al.* (ArgoNeuT Collaboration), Improved Limits on Millicharged Particles Using the ArgoNeuT Experiment at Fermilab, Phys. Rev. Lett. **124**, 131801 (2020).

[27] S. Foroughi-Abari, F. Kling, and Y. D. Tsai, Looking forward to millicharged dark sectors at the LHC, Phys. Rev. D **104**, 035014 (2021).

[28] A. Berlin, N. Blinov, G. Krnjaic, P. Schuster, and N. Toro, Dark matter, millicharges, axion and scalar particles, gauge bosons, and other new physics with LDMX, Phys. Rev. D **99**, 075001 (2019).

[29] G. Afek, F. Monteiro, J. Wang, B. Siegel, S. Ghosh, and D. C. Moore, Limits on the abundance of millicharged particles bound to matter, Phys. Rev. D **104**, 012004 (2021).

[30] E. Gabrielli, L. Marzola, E. Milotti, and H. Veermäe, Polarization observables for millicharged particles in photon collisions, Phys. Rev. D **94**, 095014 (2016); **95**, 119903(E) (2017).

[31] D. C. Moore, A. D. Rider, and G. Gratta, Search for Millicharged Particles Using Optically Levitated Microspheres, Phys. Rev. Lett. **113**, 251801 (2014).

[32] A. Berlin and A. Hook, Searching for millicharged particles with superconducting radio-frequency cavities, Phys. Rev. D **102**, 035010 (2020).

[33] R. Harnik, R. Plestid, M. Pospelov, and H. Ramani, Millicharged cosmic rays and low recoil detectors, Phys. Rev. D **103**, 075029 (2021).

[34] A. D. Dolgov and A. S. Rudenko, Relic abundance of MeV millicharged particles, J. Exp. Theor. Phys. **124**, 564 (2017).

[35] J. T. Li and T. Lin, Dynamics of millicharged dark matter in supernova remnants, Phys. Rev. D **101**, 103034 (2020).

[36] A. Aboubrahim, P. Nath, and Z. Y. Wang, A cosmologically consistent millicharged dark matter solution to the EDGES anomaly of possible string theory origin, J. High Energy Phys. 12 (2021) 148.

[37] S. Davidson, S. Hannestad, and G. Raffelt, Updated bounds on millicharged particles, J. High Energy Phys. 05 (2000) 003.

[38] H. Vogel and J. Redondo, Dark radiation constraints on minicharged particles in models with a hidden photon, J. Cosmol. Astropart. Phys. 02 (**2014**) 029.

[39] A. Caputo, L. Sberna, M. Frias, D. Blas, P. Pani, L. Shao, and W. Yan, Constraints on millicharged dark matter and axionlike particles from timing of radio waves, Phys. Rev. D **100**, 063515 (2019).

[40] M. Korwar and A. M. Thalapillil, Novel astrophysical probes of light millicharged fermions through schwinger pair production, J. High Energy Phys. 04 (2019) 039.

[41] D. Ejlli, Millicharged fermion vacuum polarization in a cosmic magnetic field and generation of CMB elliptic polarization, Phys. Rev. D **96**, 023540 (2017).

[42] X. Huang, X. P. Zheng, W. H. Wang, and S. Z. Li, Constraints on millicharged particles by neutron stars, Phys. Rev. D **91**, 123513 (2015).

[43] A. D. Dolgov, S. L. Dubovsky, G. I. Rubtsov, and I. I. Tkachev, Constraints on millicharged particles from Planck data, Phys. Rev. D **88**, 117701 (2013).

[44] A. Melchiorri, A. Polosa, and A. Strumia, New bounds on millicharged particles from cosmology, Phys. Lett. B **650**, 416 (2007).

[45] S. L. Dubovsky, D. S. Gorbunov, and G. I. Rubtsov, Narrowing the window for millicharged particles by CMB anisotropy, JETP Lett. **79**, 1 (2004).

[46] C. A. Argüelles Delgado, K. J. Kelly, and V. Muñoz Albornoz, Millicharged particles from the heavens: Single- and multiple-scattering signatures, J. High Energy Phys. 11 (2021) 099.

[47] M. Kachelriess and J. Tjemsland, Meson production in air showers and the search for light exotic particles, Astropart. Phys. **132**, 102622 (2021).

[48] R. Plestid, V. Takhistov, Y. D. Tsai, T. Bringmann, A. Kusenko, and M. Pospelov, New constraints on millicharged particles from cosmic-ray production, Phys. Rev. D **102**, 115032 (2020).

[49] L. Singh *et al.* (TEXONO Collaboration), Constraints on millicharged particles with low threshold germanium detectors at Kuo-Sheng reactor neutrino laboratory, Phys. Rev. D **99**, 032009 (2019).

[50] J. W. Chen, H. C. Chi, H. B. Li, C. P. Liu, L. Singh, H. T. Wong, C. L. Wu, and C. P. Wu, Constraints on millicharged neutrinos via analysis of data from atomic ionizations with germanium detectors at sub-keV sensitivities, Phys. Rev. D **90**, 011301 (2014).

[51] S. N. Gninenko, N. V. Krasnikov, and A. Rubbia, Search for millicharged particles in reactor neutrino experiments: A probe of the PVLAS anomaly, Phys. Rev. D **75**, 075014 (2007).

[52] S. N. Gninenko, D. V. Kirpichnikov, and N. V. Krasnikov, Probing millicharged particles with NA64 experiment at CERN, Phys. Rev. D **100**, 035003 (2019).

[53] A. A. Prinz, R. Baggs, J. Ballam, S. Ecklund, C. Fertig, J. A. Jaros, K. Kase, A. Kulikov, W. G. J. Langeveld, R. Leonard *et al.*, Search for Millicharged Particles at SLAC, Phys. Rev. Lett. **81**, 1175 (1998).

[54] A. A. Prinz, The search for millicharged particles at SLAC, Report No. SLAC-R-569.

[55] P. A. Zyla *et al.* (Particle Data Group), Review of Particle Physics, Prog. Theor. Exp. Phys. **2020**, 083C01 (2020).

[56] V. N. Bayer, V. M. Katkov, and V. S. Fadin, *Radiation of Relativistic Electrons* (Atomizdat, Moscow, 1973).

[57] A. Belyaev, N. D. Christensen, and A. Pukhov, CalcHEP 3.4 for collider physics within and beyond the standard model, Comput. Phys. Commun. **184**, 1729 (2013).

[58] X. Chu, J. Pradler, and L. Semmelrock, Light dark states with electromagnetic form factors, Phys. Rev. D **99**, 015040 (2019).

[59] S. N. Gninenko, Search for MeV dark photons in a light-shining-through-walls experiment at CERN, Phys. Rev. D **89**, 075008 (2014).

[60] E. Depero, D. Banerjee, V. Burtsev, A. Chumakov, D. Cooke, A. V. Dermenev, S. V. Donskov, F. Dubinin, R. R. Dusaev, S. Emmenegger *et al.*, High purity 100 GeV electron identification with synchrotron radiation, Nucl. Instrum. Methods Phys. Res., Sect. A **866**, 196 (2017).

[61] D. Banerjee, V. E. Burtsev, A. G. Chumakov, D. Cooke, P. Crivelli, E. Depero, A. V. Dermenev, S. V. Donskov, R. R. Dusaev, T. Enik *et al.*, Dark Matter Search in Missing Energy Events with NA64, Phys. Rev. Lett. **123**, 121801 (2019).

[62] D. Banerjee *et al.* (NA64 Collaboration), Search for Invisible Decays of sub-GeV Dark Photons in Missing-Energy Events at the CERN SPS, Phys. Rev. Lett. **118**, 011802 (2017).

[63] H. Sieber, D. Banerjee, P. Crivelli, E. Depero, S. N. Gninenko, D. V. Kirpichnikov, M. M. Kirsanov, V. Poliakov, and L. Molina Bueno, Prospects in the search for a new light Z' boson with the NA64μ experiment at the CERN SPS, Phys. Rev. D **105**, 052006 (2022).

[64] D. V. Kirpichnikov, H. Sieber, L. M. Bueno, P. Crivelli, and M. M. Kirsanov, Probing hidden sectors with a muon beam: Total and differential cross sections for vector boson production in muon Bremsstrahlung, Phys. Rev. D **104**, 076012 (2021).

[65] Y. Kahn, G. Krnjaic, N. Tran, and A. Whitbeck, M^3: A new muon missing momentum experiment to probe $(g-2)_\mu$ and dark matter at Fermilab, J. High Energy Phys. 09 (2018) 153.

[66] R. Capdevilla, D. Curtin, Y. Kahn, and G. Krnjaic, Systematically testing singlet models for $(g-2)_\mu$, J. High Energy Phys. 04 (2022) 129.

[67] P. Schuster, N. Toro, and K. Zhou, Probing invisible vector meson decays with the NA64 and LDMX experiments, Phys. Rev. D **105**, 035036 (2022).

[68] L. A. Anchordoqui, A. Ariga, T. Ariga, W. Bai, K. Balazs, B. Batell, J. Boyd, J. Bramante, M. Campanelli, A. Carmona *et al.*, The forward physics facility: Sites, experiments, and physics potential, Phys. Rep. **968**, 1 (2022).